

A Bayesian Method for Accelerated Magnetic Resonance Elastography of the Liver

THESIS

Presented in Partial Fulfillment of the Requirements for the Degree Master of Science in  
the Graduate School of The Ohio State University

By

Christopher Ebersole

Graduate Program in Electrical and Computer Engineering

The Ohio State University

2017

Master's Examination Committee:

Dr. Rizwan Ahmad, Advisor

Dr. Arunark Kolipaka, Advisor

Copyright

Christopher Ebersole

2017

## Abstract

Liver fibrosis, a common feature of many chronic liver diseases, is associated with an increase in liver stiffness. While biopsy is the clinical standard for staging fibrosis, this invasive procedure is prone to error and places the patient at risk for health complications. Magnetic resonance elastography (MRE) is a noninvasive clinical tool for staging liver fibrosis. However, MRE requires patients to perform lengthy breath holds exceeding 15 seconds for each slice in each encoding direction, which limits its clinical application. Therefore, we propose a new data acquisition and processing method to reduce MRE scan time.

The proposed method, called Bayesian method for magnetic resonance Elastography using Approximate Message passing (BEAM) utilizes a combination of several features to accelerate reconstruction. Pseudorandom sampling of k-space promotes incoherent aliasing, which allows compressive recovery via enforcement of sparsity in wavelet domain. Additionally, a spatially varying magnitude constraint is applied across offsets and polarities to exploit structure unique to MRE. BEAM is validated using

retrospectively downsampled phantom data and prospectively downsampled in vivo liver data ( $n = 86$ ).

Analysis of BEAM reconstructions demonstrate accurate quantification of mean liver stiffness up to an acceleration factor of  $R = 6$ . Bland Altman analysis indicates that BEAM ( $R = 6$ ) has a bias of  $-0.04$  kPa and limits of agreement of  $-0.36 - +0.28$  kPa when compared to the clinical standard liver MRE technique with traditional GRAPPA ( $R = 1.4$ ). This study demonstrates that by exploiting spatial sparsity and magnitude consistency, it is feasible to reduce the scan time of liver MRE by an additional factor of 4 while maintaining accurate mean stiffness quantification. This potentially enables collection of four liver slices, as per clinical protocol, within a single breath hold.

To my parents, for their sacrifices, love, and support.

## Acknowledgments

In working on this thesis I have benefitted from the support of many individuals. First, I would like to thank my advisors, Dr. Rizwan Ahmad and Dr. Arunark Kolipaka, for sharing their knowledge and encouragement as they have guided me throughout my time as a graduate student. I would also like to thank Dr. Lee Potter and Adam Rich for sharing their expertise with ReVEAL, and for providing valuable feedback on my work; Brian Raterman, for providing training and advice on conducting MRI scans; and all the members of the MRE Lab at OSU, for their friendship and assistance. Additionally, I have had the pleasure of working with numerous selfless individuals willing to volunteer their time to participate in this study. Finally, I would like to thank my family and friends for their unwavering support over the years. This accomplishment would not have been possible without them.

This work was funded by NIH grants R01HL124096 and R21EB021655.

## Vita

2015.....B.S. Electrical and Computer Engineering,  
The Ohio State University

2015 to present.....Graduate Research Associate,  
Department of Radiology,  
The Ohio State University  
Wexner Medical Center

### Fields of Study

Major Field: Electrical and Computer Engineering

## Table of Contents

Abstract.....	ii
Acknowledgments.....	v
Vita.....	vi
List of Figures.....	x
Chapter 1: Introduction.....	1
Chapter 2: Clinical Motivation.....	4
Liver Biopsy.....	4
Noninvasive Techniques.....	6
Ultrasound.....	7
Magnetic Resonance Imaging.....	8

Chapter 3: Magnetic Resonance Elastography .....	10
Chapter 4: Theory .....	16
Notation.....	16
MRE Signal Model .....	16
Bayesian Model .....	20
Wavelet Compression .....	23
Belief Propagation .....	24
Chapter 5: Methods.....	27
Retrospectively Accelerated Phantom MRE Acquisition and Reconstruction.....	28
Prospectively Accelerated In Vivo Liver MRE Acquisition and Reconstruction	28
Parameter Selection .....	30
MRE Inversion.....	31
Reconstruction Quality Metrics .....	31
Chapter 6: Results .....	33

Retrospectively Accelerated Phantom MRE Results.....	33
Prospectively Accelerated In Vivo Liver MRE Results .....	36
Chapter 7: Discussion .....	40
Chapter 8: Conclusion.....	46
References .....	47

## List of Figures

<b>Figure 1:</b> Micrograph of liver with NAFLD.....	5
<b>Figure 2:</b> Micrograph of liver with hepatocellular carcinoma.....	6
<b>Figure 3:</b> Three principle steps of MRE .....	11
<b>Figure 4:</b> Example VISTA sampling pattern .....	18
<b>Figure 5:</b> Mixture density .....	23
<b>Figure 6:</b> Factor graph representation of the joint posterior distribution.....	26
<b>Figure 7:</b> Experimental setup for liver MRE imaging. ....	29
<b>Figure 8:</b> Comparison of SENSE, SCS, and BEAM phantom reconstructions.....	34
<b>Figure 9:</b> MSE of reconstructed phantom images .....	35
<b>Figure 10:</b> Mean phantom stiffness .....	35

**Figure 11:** Comparison of GRAPPA at  $R = 1.4$  and BEAM at  $R = 1, 4, 6,$  and  $8$  ..... 37

**Figure 12:** Bland Altman analysis of BEAM-derived stiffness measurements to  
GRAPPA-derived stiffness measurements. .... 38

**Figure 13:** Bland Altman analysis of stiffness measurements derived from two separate  
GRAPPA scans. .... 39

## Chapter 1: Introduction

Soft tissue stiffness serves as a biomarker for numerous pathological conditions, including hepatic, cardiac, breast, and skeletal muscle diseases. While invasive biopsy is the current gold standard for measurement of tissue mechanical properties, this procedure introduces the potential for a variety of complications. Thus, noninvasive alternatives are preferred.

Magnetic resonance elastography (MRE) is a noninvasive procedure which estimates the shear modulus of soft tissue (1–10). MRE has demonstrated success in clinical diagnosis of hepatic fibrosis and cirrhosis. Oscillating mechanical waves are introduced to the anatomy of interest, while motion encoding gradients capture the resulting tissue motion. A series of MR images acquired at varying offsets between the motion encoding gradients and the mechanical waves are used to create a spatial map of shear stiffness, known as an elastogram. This procedure has demonstrated a high degree of accuracy in staging hepatic fibrosis (11,12). Yet even when parallel imaging techniques are applied, acquisition of this series of images requires prohibitively long breath holds.

In this work, we propose a new method, called Bayesian method for magnetic resonance Elastography using Approximate Message passing (BEAM). This method permits accelerated acquisition of MRE datasets by incorporating elements of parallel imaging and compressed sensing, and additionally through exploiting a structure unique to MRE by applying a magnitude constraint across offsets. Implementation of this constraint as a mixture density conditioned on a hidden indicator variable enables the algorithm to automatically segment the reconstructed image into regions of strong and weak magnitude consistency, applying the appropriately strong magnitude for each image pixel. This method is validated in retrospectively accelerated phantom data and 86 prospectively accelerated in vivo datasets from 23 volunteers.

The remainder of this thesis is structured as follows:

- Chapter 2 explores the clinical motivation for MRE
- Chapter 3 introduces technical considerations and limitations of MRE
- Chapter 4 describes the various aspects of BEAM, including derivation of the method and identification of tuning parameters and simplifications
- Chapter 5 describes the experimental methods used to validate BEAM in phantom and in vivo datasets
- Chapter 6 presents experimental results
- Chapter 7 provides discussion of the experimental results

- Chapter 8 summarizes the benefits and limitations of BEAM, and provides a conclusion

## Chapter 2: Clinical Motivation

Hepatic fibrosis is the accumulation of collagen in the liver (known to increase liver stiffness) caused by a variety of diseases and conditions, including chronic alcoholism, nonalcoholic fatty liver disease (NAFLD, depicted in **Figure 1**), and nonalcoholic steatohepatitis (NASH) (13–15). Late stage fibrosis, known as cirrhosis, is accompanied by distortion of the hepatic vasculature, impeding the ability of the liver to function and potentially leading to portal hypertension and hepatocellular carcinoma (shown in **Figure 2**) (16). According to a 2014 report by the U.S. Department of Health and Human Services, chronic liver disease and cirrhosis comprised the 12<sup>th</sup> leading cause of mortality in the United States, resulting in 38,170 deaths (17). Thus, substantial need exists for reliable early stage diagnosis to allow treatment and monitoring of disease progression.

### Liver Biopsy

Currently, biopsy is the gold standard in assessing liver fibrosis. Despite its widespread acceptance, numerous factors limit the efficacy of this invasive procedure. A

percutaneous liver biopsy samples 1/50,000 of the liver, or 0.002% of the liver (18). However, fibrosis is heterogeneously distributed in the liver. As a result, sampling errors of between 25% to 40% have been reported (19–21). Additionally, variation between the interpretation of biopsy results yield staging errors as high as 20% (19). The procedure has been demonstrated to cause transient pain in approximately 30% of all patients, with severe complications occurring in 3%, and mortality occurring in 0.03% of all patients (22). In addition to significant direct costs, patients experience indirect costs due to loss of productivity during recovery, with extended hospital stays required for 1-5% of patients (18).

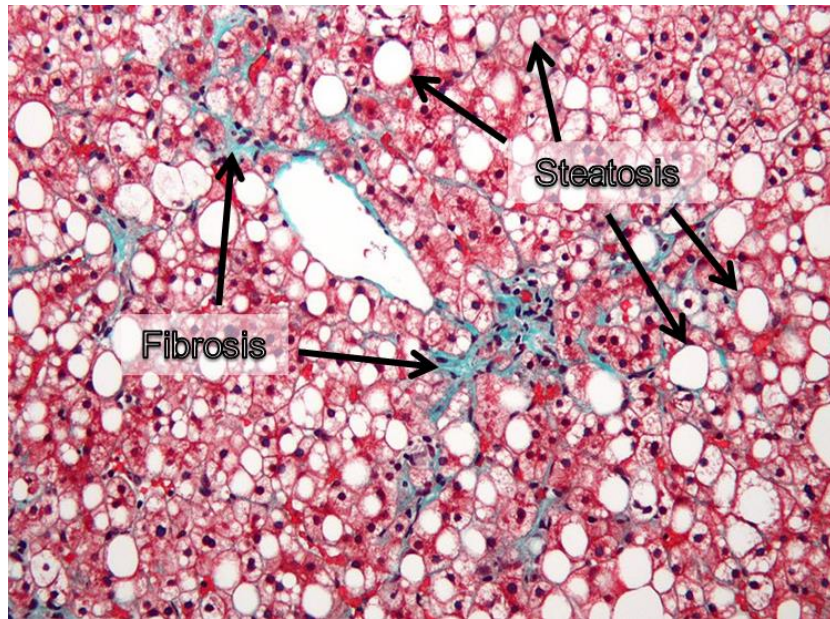


**Figure 1:** Micrograph of liver with NAFLD. Prominent macrovesicular steatosis (white oval spaces) and mild fibrosis (green) is present. © Michael Bonert, shared per CC-BY-SA-3.0.

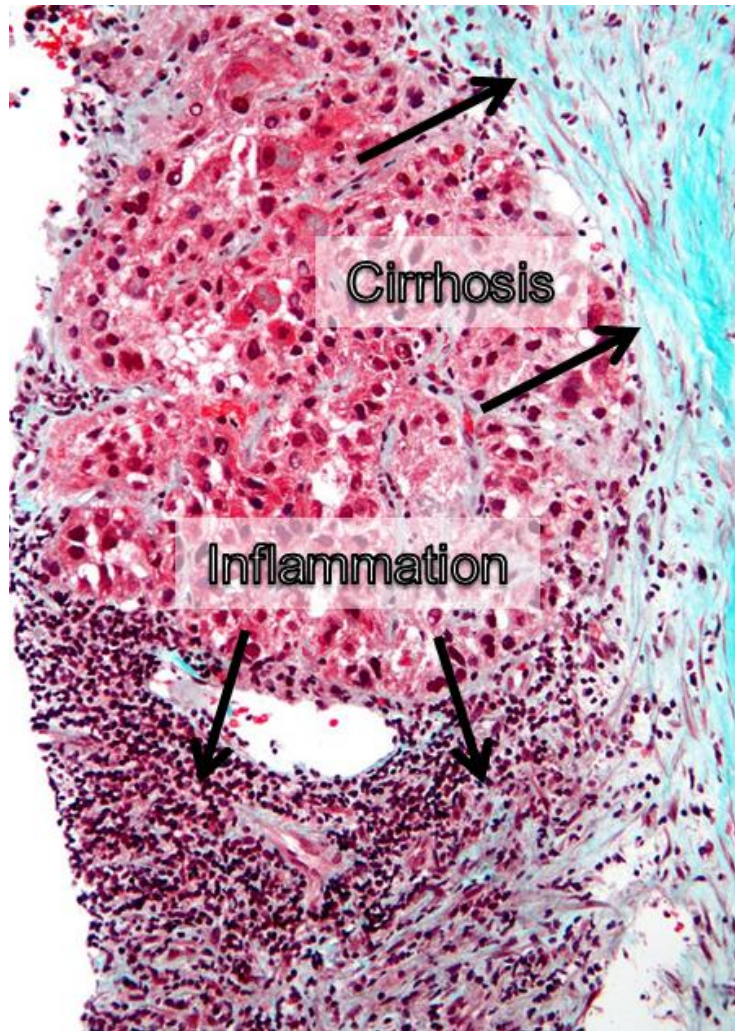


**Figure 2:** Micrograph of liver with hepatocellular carcinoma. End stage cirrhosis (green) and inflammation around the hepatic portal (lower portion) are shown. © Michael Bonert, shared per CC-BY-SA-3.0.

## Noninvasive Techniques

Several noninvasive methods exist for staging liver fibrosis and cirrhosis, including methods which utilize the ultrasound and magnetic resonance imaging modalities.

## Ultrasound

A variety of techniques exist which utilize ultrasound to stage liver fibrosis. Ultrasound imaging can be used to provide insight into morphological changes in the liver associated with advanced liver fibrosis. Hepatic vein wall morphology and liver surface nodularity have both demonstrated success as indicators of cirrhosis (23,24). However, a number of challenges limit the accuracy of morphological staging of fibrosis. Liver parenchymal texture is a subjective measure, yielding a low sensitivity and specificity. Optimal evaluation requires the presence of ascites to provide a fluid-tissue interface. This implies the fibrosis has reached an advanced stage, reducing the ability of morphological imaging to diagnose early-stage fibrosis

In addition to morphological grading, ultrasound elastography can estimate the stiffness of the liver. Several variations of ultrasound elastography exist, including transient elastography (TE), which relies on an external transducer to introduce mechanical shear waves into the region of interest, while ultrasound is used to measure the propagation velocity of the shear waves, yielding the stiffness of the tissue (25). A pooled meta-analysis of TE studies by Friedrich-Rust et al. (26) yielded a mean area under the receiver operating characteristic curve (AUROC) of 0.84 (95% confidence interval [CI] 0.82-0.86) for significant fibrosis, 0.89 (95% CI 0.88-0.91) for severe fibrosis, and 0.94 (95% CI 0.93-0.95) for cirrhosis. Alternatively, acoustic force radiation impulse (ARFI) utilizes a short duration ultrasound pulse to displace tissue before monitoring the propagation of

the resulting shear wave (23). A meta-analysis of ARFI studies by Friedrich-Rust et al. in (27) yielded an AUROC of 0.87 (95% CI 0.83-0.92) for significant fibrosis, 0.91 (95% CI 0.86-0.96) for severe fibrosis, and 0.93 (95% CI 0.89-0.97) for cirrhosis.

While ultrasound-based methods provide a low cost alternative to invasive biopsy, these methods suffer from a number of disadvantages. Ultrasound imaging suffers from limited acoustic wave penetration due to signal attenuation in tissue, and thus is unable to image structures located deep within a patient. This poses a particular challenge in imaging obese patients. Furthermore, ultrasound is user dependent, requiring technicians to undergo extensive training. Additionally, the ultrasound elastography systems produced by different vendors yield varying results, and thus establishment of threshold values for staging fibrosis has been difficult (28). Finally, ultrasound elastography exhibits less accuracy than magnetic resonance elastography, as discussed below.

## Magnetic Resonance Imaging

Magnetic resonance imaging (MRI) is a powerful imaging modality that addresses a number of the shortcomings of ultrasound, including access to structures located deep within patients. As with ultrasound imaging, MRI can be used to assess liver morphology. MRI additionally permits encoding of alternative tissue features. For example, MRI-based diffusion weighted imaging (DWI) measures the rate of diffusion of water molecules in tissue. It has been observed that liver with cirrhosis yields restricted

diffusion (29). A meta-analysis of DWI studies by Wang et al. in (30) yielded an AUROC of 0.86 (95% CI 0.83-0.89) for stage 1 fibrosis, 0.83 (0.79-0.86) for stage 2 fibrosis, and 0.86 (0.83-0.89) for stage 3 fibrosis. Alternatively, magnetic resonance elastography (MRE) estimates soft tissue stiffness through phase-contrast MRI by motion encoding of externally applied shear waves. A pooled meta-analysis of MRE in (30) yielded an AUROC of 0.95 (95% CI 0.93-0.97) for stage 1 fibrosis, 0.98 (95% CI 0.97-0.99) for stage 2 fibrosis, 0.98 (95% CI 0.96-0.99) for stage 3 fibrosis, and 0.99 (95% CI 0.97-0.99) for cirrhosis. Thus, MRE yields the highest degree of accuracy for staging fibrosis of all the noninvasive methods investigated. Additionally, MRE is highly accurate at staging fibrosis at early stages of the disease. An introduction to the technical aspects of MRE is given in chapter 3.

## Chapter 3: Magnetic Resonance Elastography

Magnetic resonance elastography (MRE) has emerged as a noninvasive, quantitative method of measuring the stiffness of soft tissue (1,31–41). MRE has found clinical application in the diagnosis of hepatic fibrosis and cirrhosis (12,42–44) and demonstrates potential in diagnosing various other hepatic, cardiac, brain, breast, aorta and skeletal muscle diseases (2–10). MRE consists of three principal steps, as shown in **Figure 3**. First, the region of interest is interrogated with mechanical waves. Next, the mechanical waves are encoded into the phase of the complex MR image signal. Finally, an MRE inversion algorithm is applied to the MRI phase images to produce a quantitative spatial map of the shear modulus, known as an elastogram.

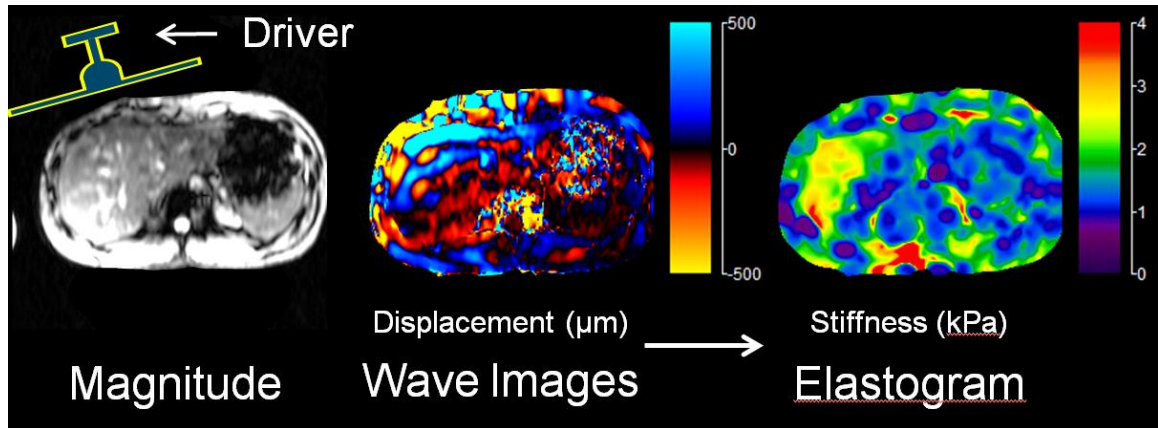


**Figure 3:** Three principle steps of MRE, including introduction of mechanical waves via an external driver, encoding the resulting motion into the phase of the complex-valued images, and creation of an elastogram via an MRE inversion algorithm.

The mechanical waves used in MRE are generated by an acoustic transducer and then routed to an MR safe passive driver placed above the anatomy of interest. A variety of driver architectures exist, including electromechanical, piezoelectric, and pneumatic drivers, with differing advantages and disadvantages (31). The frequency of these interrogating waves typically ranges from 50 – 500 Hz. Higher frequency mechanical waves yield greater sensitivity to anatomic motion due to the smaller applied wavelength, while lower frequencies demonstrate greater resistance to attenuation, extending the penetration depth of the waves.

The resulting oscillatory motion of the anatomy is encoded into the phase of the complex MR images through application of a motion encoding gradient (MEG). These gradients can be applied in one or more directions in a standard MRI pulse sequence. The resulting

phase accumulated by the MR signal at position  $\mathbf{r}$  and phase offset  $\theta$  between the motion and the MEG is expressed using the following equation (31)

$$\phi(\mathbf{r}, \theta) = \frac{\gamma NT \langle \mathbf{G}, \xi_0 \rangle}{2} \cos(\langle \mathbf{k}, \mathbf{r} \rangle + \theta) \quad (1)$$

where  $\gamma$  is the gyromagnetic ratio of hydrogen,  $N$  is the number of gradient pairs used to sensitize the motion,  $T$  is the period of the MEG,  $\mathbf{G}$  is the amplitude of the MEG,  $\xi_0$  is the maximum amplitude of the motion, and  $\mathbf{k}$  is the wave number. Thus, the phase of the MR signal is proportional to the tissue displacement.

While the displacement of the anatomy due to the applied mechanical waves is small, synchronization of the MEG with the waves results in significant accumulation of phase. The effects of background phase are eliminated by repeating this acquisition with an MEG of the opposite polarity, allowing differentiation of the motion-encoded phase and background phase. A series of motion-encoded images are acquired at various phase offsets between the MEG and the mechanical motion, characterizing the wave propagation through the region of interest.

After the complex-valued images are reconstructed for each offset, one of several MRE inversion algorithms is applied to produce a spatial map of the shear modulus, known as an elastogram. Most of the current inversion algorithms are based on the Helmholtz wave equation, as shown in equation 1 of (45), for planar waves propagating in a uniform,

homogeneous, isotropic medium. Local frequency estimation (LFE) produces a local estimate of the instantaneous frequency of the mechanical waves after application of lognormal quadrature filters (45,46) in the spatial frequency domain of the first harmonic displacement field. Alternatively, multimodel direct inversion (MMDI) attempts to fit low order polynomials to the first harmonic displacement field in a finite processing window (47,48) to estimate the Laplacian for solving the Helmholtz wave equation.

MRE can be performed in two or three spatial dimensions and with up to three orthogonal motion encoding directions. In practice, however, volumetric acquisitions with multi-directional encodings are not utilized due to prohibitively long acquisition times. Even low-resolution planar imaging with a single encoding direction, when used in conjunction with parallel MRI (pMRI), typically requires a long breath hold (> 15 seconds). To avoid excessive noise amplification, it is a common practice to use pMRI with only modest acceleration rates ( $R < 2$ ). To improve clinical utility of MRE and to enable volumetric measurements, it is necessary to accelerate the MRE acquisition while maintaining the accuracy of stiffness quantification.

Compressive sensing (CS) has been successfully employed to recover images at high acceleration rates for several MRI applications (49–53), yet its potential has not yet been recognized for MRE reconstruction. CS enables recovery from highly undersampled data by exposing and exploiting the underlying compressibility of the image. Three conditions must be met to exploit CS. First, the image must be sparse, or contain few nonzero

elements, in some transform domain. Sparsity refers to the number of transform coefficients necessary to form a close approximate representation of the image. Second, the sampling pattern used must generate incoherent aliasing under the sparsifying transform. Finally, application of a nonlinear reconstruction which enforces both measurement fidelity and sparsity of the transform image representation enables recovery from highly undersampled data. More recently, Rich et al. (54) proposed a Bayesian method, called ReVEAL, to highly accelerate phase-contrast MRI. ReVEAL goes beyond the concept of utilizing sparsity and additionally exploits magnitude and phase structure unique to phase-contrast MRI.

In chapter 4, we propose a new method, called Bayesian method for magnetic resonance Elastography using Approximate Message passing (BEAM), which permits significant acceleration of MRE via Bayesian modelling. BEAM can be considered an adaptation of ReVEAL. BEAM, like traditional CS methods, employs pseudorandom sampling and exploits spatial sparsity in the image at each offset. In contrast to traditional CS methods, the proposed approach also exploits structure unique to MRE. To that end, BEAM enforces magnitude consistency across different offsets through implementation of a mixture density and hidden indicator variable that automatically controls the strength of magnitude consistency for a given pixel.

The aim of this study is to develop and validate BEAM against the clinical standard MRE sequence for staging liver fibrosis in a standard MRE phantom with known stiffness and in volunteers for estimating liver stiffness.

## Chapter 4: Theory

### Notation

We adopt the following notation. Vectors and matrices are represented in bold, with matrices represented by capital letters. Elements of matrices are denoted  $a_{ij}$  for the  $i^{\text{th}}$  row and  $j^{\text{th}}$  column of  $\mathbf{A}$ , while  $x_i$  indicates the  $i^{\text{th}}$  element of vector  $\mathbf{x}$ . For vectors identified by subscripts, vector elements are designated by a second subscript, such as  $x_{0_1}$  representing the 1<sup>st</sup> element of vector  $\mathbf{x}_0$ . Elementwise multiplication of vectors is denoted  $\mathbf{a} \times \mathbf{b}$ . The  $n$ -by- $n$  identity matrix is expressed as  $\mathbf{I}_n$ . Finally,  $\mathcal{CN}(x; \mu, \sigma^2)$  represents a circularly symmetric complex Gaussian distribution on random variable  $x$  with mean  $\mu$  and variance  $\sigma^2$ .

### MRE Signal Model

The raw MRI signal acquired by the  $c^{\text{th}}$  coil of a receiver array for the  $j^{\text{th}}$  offset between the mechanical oscillation and the motion encoding gradient can be expressed as

$$\mathbf{y}_j^c = \mathbf{D}_j \mathcal{F} \mathbf{S}^c \mathbf{x}_j + \boldsymbol{\eta}_j^c, \quad (2)$$

where  $\mathbf{S}^c$  is the coil sensitivity encoding matrix for coil  $c = 0, 1, \dots, C - 1$ ,  $\mathcal{F}$  is the Fourier transform, and  $\mathbf{D}_j$  is the sample selection operator for offset  $j$ . Here,  $\mathbf{x}_j \in \mathbb{C}^N$  is the complex-valued image to be recovered for the  $j^{\text{th}}$  offset,  $\boldsymbol{\eta}_j^c \in \mathbb{C}^M$  is complex-valued, zero-mean Gaussian noise with variance  $\omega^2$ ,  $\mathbf{y}_j^c \in \mathbb{C}^M$  is the measured complex-valued data, and  $j = 0, 1, \dots, J - 1$  represent  $J$  different offsets. The measurements for a multi-coil acquisition with  $C$  total coils can therefore be represented as

$$\begin{bmatrix} \mathbf{y}_j^0 \\ \mathbf{y}_j^1 \\ \vdots \\ \mathbf{y}_j^{C-1} \end{bmatrix} = \begin{bmatrix} \mathbf{D}_j \mathcal{F} \mathbf{S}^0 \\ \mathbf{D}_j \mathcal{F} \mathbf{S}^1 \\ \vdots \\ \mathbf{D}_j \mathcal{F} \mathbf{S}^{C-1} \end{bmatrix} \mathbf{x}_j + \begin{bmatrix} \boldsymbol{\eta}_j^0 \\ \boldsymbol{\eta}_j^1 \\ \vdots \\ \boldsymbol{\eta}_j^{C-1} \end{bmatrix}, \quad (3)$$

Thus, by defining  $\mathbf{A}_j$  as the encoding matrix above, the signal acquired for the  $j^{\text{th}}$  offset can be written as

$$\mathbf{y}_j = \mathbf{A}_j \mathbf{x}_j + \boldsymbol{\eta}_j, \quad (4)$$

where  $\mathbf{y}_j \in \mathbb{C}^{MC}$  and  $\boldsymbol{\eta}_j \in \mathbb{C}^{MC}$  are obtained by concatenating  $\mathbf{y}_j^c$  and  $\boldsymbol{\eta}_j^c$ , respectively, from all coils.

To promote incoherent aliasing, a variable density pseudorandom sampling pattern called variable density incoherent spatiotemporal acquisition (VISTA) was employed (55).

Since VISTA operates in the offset-ky domain, it implicitly discourages repeated sampling of the same k-space location across different offsets, maximizing the information content of the sampled data. A typical VISTA pattern is shown in **Figure 4**, where the offset on the x-axis represents positive and negative encoding with four equally spaced samplings of the external motion required for MRE.

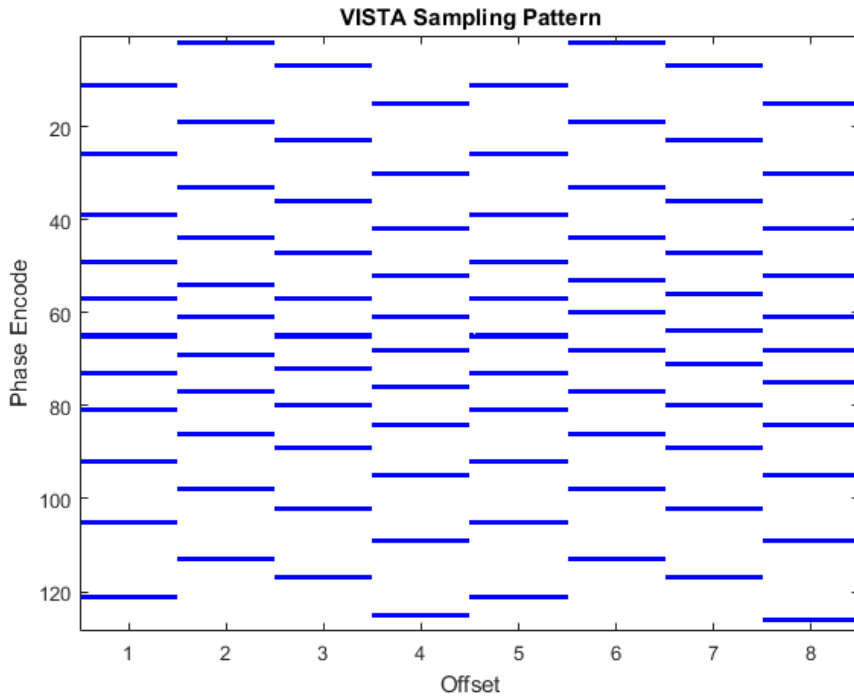


**Figure 4:** Example VISTA sampling pattern for 128 phase encodes and  $R = 11.6$ . The pattern is generated in the integrated offset-ky domain.

For MRE, we can model images at different offsets according to

$$\begin{aligned}
\mathbf{x}_0 &= \mathbf{m}_0 \times e^{i(\phi+\theta_0)} \\
\mathbf{x}_1 &= \mathbf{m}_1 \times e^{i(\phi+\theta_1)} \\
&\vdots \\
\mathbf{x}_{J-1} &= \mathbf{m}_{J-1} \times e^{i(\phi+\theta_{J-1})}, \quad (5)
\end{aligned}$$

where  $\theta_j$  is the spatially varying phase accumulated due to motion encoding for the  $j^{\text{th}}$  offset and  $\phi$  is the spatially varying reference phase incurred by magnetic field inhomogeneity and off-resonance effects. Without loss of generality, we can define  $\phi$  such that  $\theta_0 = 0$ , yielding  $\mathbf{x}_0 = \mathbf{m}_0 e^{i(\phi)}$ .

In the absence of any non-ideal behavior, one expects  $\mathbf{m}_0 = \mathbf{m}_1 = \dots = \mathbf{m}_{J-1}$ . However, due to intravoxel dephasing and other potential sources of model mismatch, the magnitudes across different offsets can vary. Since it is not known in advance which pixel (voxel) will exhibit dephasing, we introduce a pixel-wise Bernoulli map,  $\mathbf{v} \in \{0,1\}^N$ , to denote the presence (or absence) of potential magnitude discrepancy among offsets.

## Bayesian Model

Now, we write the posterior probability distribution of the unknown parameters,  $\mathbf{x}_0, \mathbf{x}_1, \mathbf{x}_2, \boldsymbol{\theta}_1, \boldsymbol{\theta}_2, \mathbf{v}$ . For notational simplification, we assume  $J = 3$ , i.e., the measurements are made at three offsets. The model, however, is amenable to any arbitrary number of offsets,  $J$ . Using Bayes' rule, the posterior distribution can be expanded as

$$\begin{aligned} p(\mathbf{x}_0, \mathbf{x}_1, \mathbf{x}_2, \boldsymbol{\theta}_1, \boldsymbol{\theta}_2, \mathbf{v} | \mathbf{y}_0, \mathbf{y}_1, \mathbf{y}_2) \\ \propto p(\mathbf{x}_0, \mathbf{x}_1, \mathbf{x}_2, \boldsymbol{\theta}_1, \boldsymbol{\theta}_2, \mathbf{v}) p(\mathbf{y}_0 | \mathbf{x}_0) p(\mathbf{y}_1 | \mathbf{x}_1) p(\mathbf{y}_2 | \mathbf{x}_2), \end{aligned} \quad (6)$$

where  $p(\mathbf{y}_j | \mathbf{x}_j)$  is the likelihood function for offset  $j$ . By invoking the chain rule, the prior in Equation 5 can be further factorized as follows.

$$\begin{aligned} p(\mathbf{x}_0, \mathbf{x}_1, \mathbf{x}_2, \boldsymbol{\theta}_1, \boldsymbol{\theta}_2, \mathbf{v}) \\ = p(\mathbf{x}_2 | \mathbf{x}_0, \mathbf{x}_1, \boldsymbol{\theta}_1, \boldsymbol{\theta}_2, \mathbf{v}) p(\mathbf{x}_1 | \mathbf{x}_0, \boldsymbol{\theta}_1, \boldsymbol{\theta}_2, \mathbf{v}) p(\boldsymbol{\theta}_1 | \mathbf{x}_0, \boldsymbol{\theta}_2, \mathbf{v}) p(\boldsymbol{\theta}_2 | \mathbf{x}_0, \mathbf{v}) p(\mathbf{v} | \mathbf{x}_0) p(\mathbf{x}_0), \end{aligned} \quad (7)$$

This model is greatly simplified by adopting several independence assumptions. First, it is assumed that magnitude discrepancy map  $\mathbf{v}$  is independent of the reference offset,  $\mathbf{x}_0$ , such that  $p(\mathbf{v} | \mathbf{x}_0) = p(\mathbf{v})$ . Next, it is assumed that the motion-encoded phase of each offset is independent of the magnitude and phase of each other offset and  $\mathbf{v}$ . Thus,  $p(\boldsymbol{\theta}_j | \mathbf{x}_0, \boldsymbol{\theta}_k, \mathbf{v}) = p(\boldsymbol{\theta}_j)$  for all  $k \neq j$ . Finally, it is assumed that all offset images are independent when conditioned on the reference image. Therefore,

$p(\mathbf{x}_j|\mathbf{x}_0, \mathbf{x}_k, \boldsymbol{\theta}_j, \boldsymbol{\theta}_k, \mathbf{v}) = p(\mathbf{x}_j|\mathbf{x}_0, \boldsymbol{\theta}_j, \mathbf{v})$  for all  $k \neq j$ . Consequently, the simplified prior yields

$$p(\mathbf{x}_0, \mathbf{x}_1, \mathbf{x}_2, \boldsymbol{\theta}_1, \boldsymbol{\theta}_2, \mathbf{v}) \approx p(\mathbf{x}_2|\mathbf{x}_0, \boldsymbol{\theta}_2, \mathbf{v})p(\mathbf{x}_1|\mathbf{x}_0, \boldsymbol{\theta}_1, \mathbf{v})p(\boldsymbol{\theta}_1)p(\boldsymbol{\theta}_2)p(\mathbf{v})p(\mathbf{x}_0), \quad (8)$$

The resulting posterior distribution, consisting of the likelihood functions and simplified prior, benefits from drastic reduction in computational complexity while retaining the fundamental structure relating offset images. The data model is fully characterized through selection of each of the posterior factors.

For zero-mean circularly-symmetric additive Gaussian noise, with variance  $\omega^2$ , the likelihood distributions are given by the following expression.

$$p(\mathbf{y}_j|\mathbf{x}_j) = \mathcal{CN}(\mathbf{y}_j; \mathbf{A}_j\mathbf{x}_j, \omega^2\mathbf{I}), \quad (9)$$

A constant magnitude across offsets is enforced through selection of the conditional prior distribution relating each offset to the reference offset,  $\mathbf{x}_0$ . To accommodate model mismatches which reduce the validity of the magnitude assumption, the conditional prior for offset image  $\mathbf{x}_j$  is given by the following mixture density conditioned on the magnitude discrepancy indicator,  $\mathbf{v}$ .

$$p(\mathbf{x}_j|\mathbf{x}_0, \boldsymbol{\theta}_j, \mathbf{v}) = \mathbf{v}\mathcal{CN}(\mathbf{x}_j; \mathbf{x}_0 e^{i\boldsymbol{\theta}_j}, \sigma_1^2\mathbf{I}) + (1 - \mathbf{v})\mathcal{CN}(\mathbf{x}_j; \mathbf{x}_0 e^{i\boldsymbol{\theta}_j}, \sigma_2^2\mathbf{I}), \quad (10)$$

The two components of this mixture are shown in **Figure 5**. Each term of the mixture constrains the magnitude of  $\mathbf{x}_j$  to resemble that of reference image  $\mathbf{x}_0$ , while leaving the encoded phase  $\boldsymbol{\theta}_j$  unconstrained with respect to the reference image. By selection of two differing variances for the mixture components, i.e.  $\sigma_1^2 < \sigma_2^2$ , the appropriately strong magnitude constraint can be applied locally throughout the image based on the value of the magnitude discrepancy indicator,  $\mathbf{v}$ . The prior probability of strong magnitude consistency at each pixel  $n$  is uniformly assigned as  $p(v_n = 1) = \gamma$ . For the prior on the motion-encoded phase,  $p(\boldsymbol{\theta}_j)$ , an uninformative uniform distribution is selected on the interval  $[0, 2\pi)$ .

On the one hand, the factor  $p(\mathbf{y}_j | \mathbf{x}_j)$ , represents the noise uncertainty in the MRE acquisition and provides a traditional sum-of-squares data fidelity term in the reconstruction. On the other hand, the factors in the prior, such as  $p(\boldsymbol{\theta}_j)$ ,  $p(\mathbf{v})$ , and  $p(\mathbf{x}_0)$  provide a regularization effect in image reconstruction. Thus, the various simplifying assumptions above maintain data fidelity while providing a trade-off between physically motivated regularizing constraints and computational complexity. Further, the modeling parameter  $\mathbf{v}$  provides, at each voxel, an automated tuning of the intra-offset regularization.

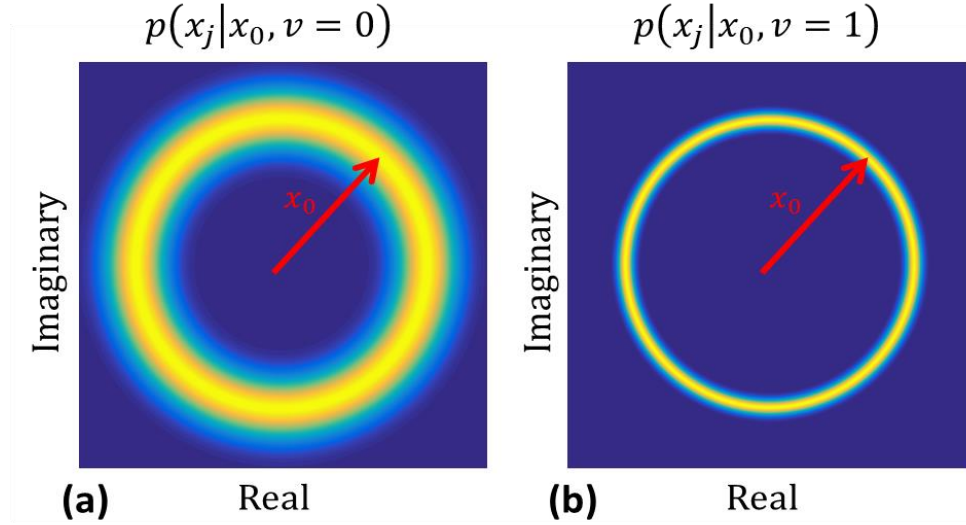


**Figure 5:** Mixture density relating offset  $\mathbf{x}_j$  to the reference offset  $\mathbf{x}_0$ . (a) The conditional distribution that enforces weak magnitude consistency, accommodating large magnitude variations across offsets, for example, due to dephasing. (b) The conditional distribution that enforces strong magnitude constraint, permitting little variation in magnitude. BEAM automatically assigns the probability that a given pixel belongs to  $\mathbf{v} = \mathbf{0}$  or  $\mathbf{v} = \mathbf{1}$  and enforces appropriate contributions from the two components of the mixture density.

## Wavelet Compression

Selection of the prior,  $p(\mathbf{x}_j)$ , on each complex-valued offset is the final remaining modelling decision to be addressed. Here, a prior is selected such that sparsity is promoted in each offset under a two-dimensional undecimated wavelet transform. To this end, we assume an analysis compressed sensing formulation, where the wavelet synthesis operator  $\Psi$  is appended as additional rows to forward operator  $\mathbf{A}_j$ , as in (56). The image

prior is defined as a zero-mean Laplace distribution on the complex-valued wavelet coefficients with shape parameter  $\lambda$ .

$$p(\mathbf{x}_j) \propto \prod_{n=0}^{N-1} \frac{\lambda^2}{2\pi} e^{-\lambda |\Psi \mathbf{x}_j|_n}, \quad (11)$$

For Gaussian likelihood and Laplace prior, the maximum a posteriori (MAP) estimate is equivalent to solving the following optimization problem.

$$\begin{aligned} \mathbf{x}_{MAP} &= \underset{\mathbf{x}}{\operatorname{argmax}} p(\mathbf{x}|\mathbf{y}) = \underset{\mathbf{x}}{\operatorname{argmax}} p(\mathbf{y}|\mathbf{x})p(\mathbf{x}) \\ &= \underset{\mathbf{x}}{\operatorname{argmax}} \ln(p(\mathbf{y}|\mathbf{x})) + \ln(p(\mathbf{x})) \\ &= \underset{\mathbf{x}}{\operatorname{argmin}} \frac{1}{\omega^2} \|\mathbf{y} - \mathbf{A}\mathbf{x}\|_2^2 + \lambda \|\Psi \mathbf{x}\|_1, \quad (12) \end{aligned}$$

Here  $\mathbf{y}$ ,  $\mathbf{x}$ , and  $\mathbf{A}$  represent the data, image, and encoding matrix, respectively, from all offsets.

## Belief Propagation

The posterior distribution of the Bayesian MRE model can be represented visually as a factor graph, as shown in **Figure 6**. Circular nodes represent random variables, while square nodes represent distributions. Edges between these nodes represent dependence of

distributions on variables. By analogy, just as the gradient of a cost function can specify an iterative algorithm, such as conjugate gradients, the factor graph can specify an iterative algorithm for determining the posterior mean image using a Bayesian model. Specifically, application of the sum-product algorithm on the factor graph provides a computationally efficient method of estimating the marginal posterior distributions of  $\mathbf{x}_j$ ,  $\boldsymbol{\theta}_j$ , and  $\mathbf{v}$  (57,58). The algorithm passes messages between nodes containing beliefs about the values of surrounding variables. The marginal posterior distributions of variables in the loop free region of the graph are exactly determined after a message is passed in each direction across each edge. In the densely interconnected regions introduced by the Fourier measurement operator the generalized approximate message passing (GAMP) algorithm is utilized to significantly reduce computational complexity through application of the central limit theorem and Taylor series approximations; GAMP leverages the large number of pixels in each offset to approximate messages as simply Gaussian (59). Once marginal posterior distributions are obtained, the maximum a posteriori estimate of each reconstruction is obtained by finding the maximum value of the distribution.

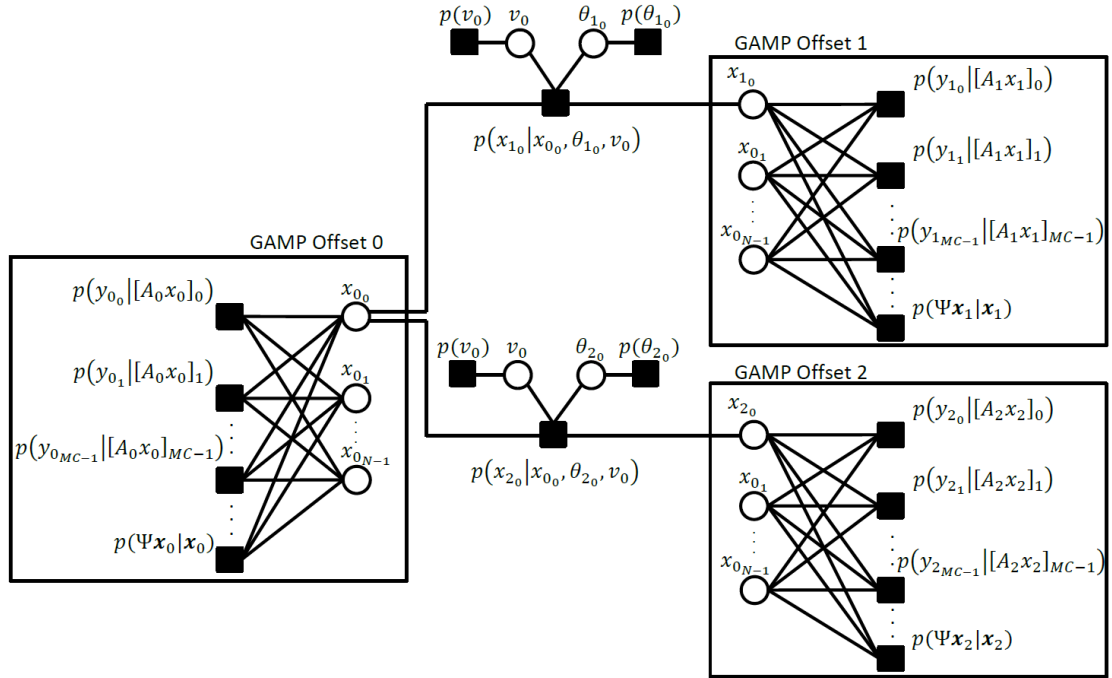


**Figure 6:** Factor graph representation of the joint posterior distribution of an MRE dataset with three offsets. This structure is expandable to an arbitrary number of offsets, retaining this structure which relates each offset to the reference offset  $\mathbf{x}_0$ . Application of an iterative message passing algorithm provides a computationally efficient method of estimating the posterior marginal distribution of variables of interest. GAMP permits rapid estimation of messages passed in the densely interconnected loopy regions of the graph, which represent each offset.

In summary, each offset image is first reconstructed from noisy measurements via GAMP. The resulting approximated messages are then passed between offset images, where a spatially varying magnitude constraint is enforced by the mixture density. The messages received by each offset image are then used to update the image estimate through an updated GAMP reconstruction. This algorithm is iterated until convergence.

## Chapter 5: Methods

The study protocol involving human subject was approved by the Institutional Review Board. Written, informed consent was obtained from each volunteer. All imaging was performed on a 3 T clinical MRI scanner (Tim Trio, Siemens Healthineers, Erlangen, Germany), using a gradient echo MRE pulse sequence. Offline reconstructions were performed in MATLAB (Mathworks, Natick, MA). Across several studies we compared BEAM to spatial CS (SCS) as well as SENSE (60) or GRAPPA (61) reconstructions. When performing BEAM and SCS reconstructions, the same VISTA sampling patterns, wavelet compression, and GAMP solver were used. However, the SCS reconstructions only exploited spatial sparsity and were performed independently on each offset image without application of any magnitude constraint jointly across offsets.

## Retrospectively Accelerated Phantom MRE Acquisition and Reconstruction

BEAM was first validated using a cylindrical phantom with known stiffness (5.6 kPa). Mechanical waves were applied to the phantom at a frequency of 60 Hz with an MEG frequency of 60 Hz. Fully sampled data were acquired on a 256x256 matrix with four MRE phase offsets with positive and negative motion encoding. The field of view was 280x280 mm<sup>2</sup>, with 5 mm slice thickness, TE = 21.9 ms, and TR = 50 ms. The data were retrospectively downsampled using a VISTA sampling pattern to allow SCS and BEAM reconstruction and a uniform sampling pattern for SENSE reconstruction at R = 1, 2, ... , 15. The central 128 lines of k-space from a single offset were used to generate coil sensitivity maps, as suggested by Walsh et al. (62). This study was also used to optimize parameters for BEAM and SCS.

## Prospectively Accelerated In Vivo Liver MRE Acquisition and Reconstruction

Liver MRE was performed on 23 healthy individuals (14 men, 9 women, mean age 26, age range 21 to 38) using an 18-channel coil array. The experimental setup is shown below in **Figure 7**. Three or four axial slices were sequentially collected for each volunteer, yielding a total of 86 axial slices. In each scan, the field of view was 320x320

mm, with 5 mm slice thickness. Data were collected on a 128x64 matrix with TE = 21.16 ms and TR = 50 ms. Mechanical waves were applied to the abdominal region at a frequency of 60 Hz while an MEG of 60 Hz was applied.

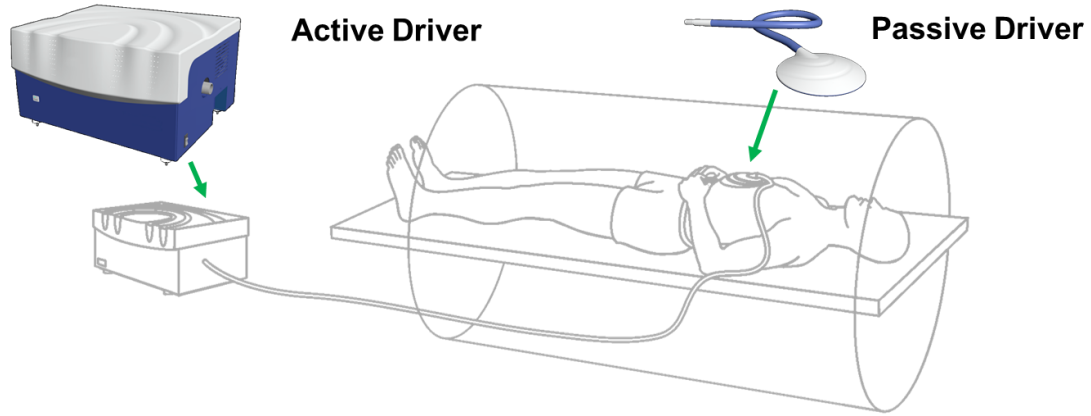


**Figure 7:** Experimental setup for liver MRE imaging.

For each slice, a low resolution pre-scan (48 lines of k-space) was acquired under a separate breath hold to generate coil sensitivity maps. The prescan was collected in the presence of mechanical vibrations and with MEG activated. Next, prospectively downsampled MRE data were acquired using a VISTA sampling pattern for R = 1, 4, 6, and 8 with four MRE phase offsets with positive and negative motion encoding, requiring breath holds of 25.6, 6.4, 4.3, and 3.2 seconds, respectively. For comparison, each slice was also acquired at R = 1.4 with 24 reference lines (18 s breath hold) and reconstructed online with GRAPPA. Additionally, repeated GRAPPA scans were acquired from 5 volunteers (19 slices) to determine the variance among GRAPPA measurements collected

under similar settings but different breath holds. BEAM and SCS reconstructions were performed offline in MATLAB on a 128x128 grid. Before each reconstruction was interpolated to 256x256 by zero padding k-space, Gaussian windowing was applied to reduce Gibbs ringing. The R = 1.4 GRAPPA acquisitions were reconstructed online on a 256x256 grid.

## Parameter Selection

Noise variance,  $\omega^2$ , was estimated from the periphery of k-space. Before processing, all data sets were normalized by a factor of  $\frac{1}{\text{mean}(|\tilde{x}|)}$ , where  $\tilde{x}$  is the reconstructed pre-scan after thresholding to eliminate low-intensity regions. The prior probability of strong magnitude consistency,  $\gamma$ , was set at 0.9 for all datasets, and moderate changes (range: 0.8—0.95) in  $\gamma$  resulted in no appreciable difference in the image quality. For phantom study, the values of the Laplace shape parameter controlling the strength of the wavelet compression,  $\lambda$ , and the mixture density variances controlling the degree of magnitude regularization,  $\sigma_1^2$  and  $\sigma_2^2$ , were manually adjusted using an additional phantom dataset (not shown). For in vivo study, the values of  $\lambda$ ,  $\sigma_1^2$ , and  $\sigma_2^2$  were manually adjusted using separate retrospectively downsampled datasets (not shown) from three volunteers.

## MRE Inversion

The phase from reconstructed complex-valued offsets was then used to generate elastograms in MRELab (Mayo Clinic, Rochester, MN). After applying a phase unwrapping algorithm, directional filtering was applied in four directions with passbands spanning 2 to 128 waves per field of view to mitigate interference from reflected mechanical waves (45). Elastograms were created for each dataset via multimodel direct inversion (MMDI) (48). Manual regions of interest (ROI) were drawn avoiding large vessels and poor wave amplitudes within the liver to report mean stiffness.

## Reconstruction Quality Metrics

Retrospectively accelerated reconstruction quality was quantified through calculation of the mean squared error (MSE), defined as

$$MSE\{\hat{\mathbf{x}}\} = 10 \log_{10} \frac{\|\hat{\mathbf{x}} - \mathbf{x}_{ref}\|_2^2}{\|\mathbf{x}_{ref}\|_2^2}, \quad (13)$$

where  $\hat{\mathbf{x}}$  is the reconstructed image and  $\mathbf{x}_{ref}$  is the fully sampled reference image. This metric provides a global measure of reconstruction quality by considering the entire complex reconstruction across all four offsets with positive and negative motion encoding.

For all studies, mean stiffness of BEAM and SCS within a user defined ROI was compared with that of SENSE (for phantom) or GRAPPA (in vivo). For phantom data, SENSE was used to reconstruct the reference images to enable MSE computation for BEAM and SCS, which are also based on a SENSE formulation. For in vivo data, GRAPPA was used as reference to emulate the existing clinical protocol. For phantom, the ROI was selected based on magnitude threshold and consisted of the entire circular cross section. For in vivo data, ROI was localized inside the liver near the driver and was manually selected by an expert user (AK, ~12 years of experience in analyzing MRE data). The mean stiffness within the ROI was then compared across reconstructions and accelerations to determine the effectiveness of each reconstruction at preserving estimated stiffness.

In the prospectively accelerated in vivo study, Bland Altman analysis was performed to assess the agreement between GRAPPA and BEAM derived stiffness estimates (63). In this analysis, the mean difference across estimates yields the overall bias of BEAM compared to GRAPPA, and the 95% limits of agreement capture the overall variance between BEAM and GRAPPA. Additionally, examination of the Bland Altman plot provides insight into the possibility of proportional bias, where the agreement between methods varies based on the average value of the measurements. Additionally, the Pearson correlation coefficient,  $r$ , was assessed between GRAPPA and BEAM derived stiffness estimates.

## Chapter 6: Results

### Retrospectively Accelerated Phantom MRE Results

A sample of phantom magnitude images, wave images, and elastograms is shown in **Figure 8** after reconstruction using SENSE, SCS, and BEAM at various accelerations.

The MSE (in dB) of each reconstruction for  $R = 1, 2, \dots, 15$  was calculated and is shown in **Figure 9**. **Figure 10** depicts the mean stiffness of the phantom, as calculated from each reconstruction using MMDI.

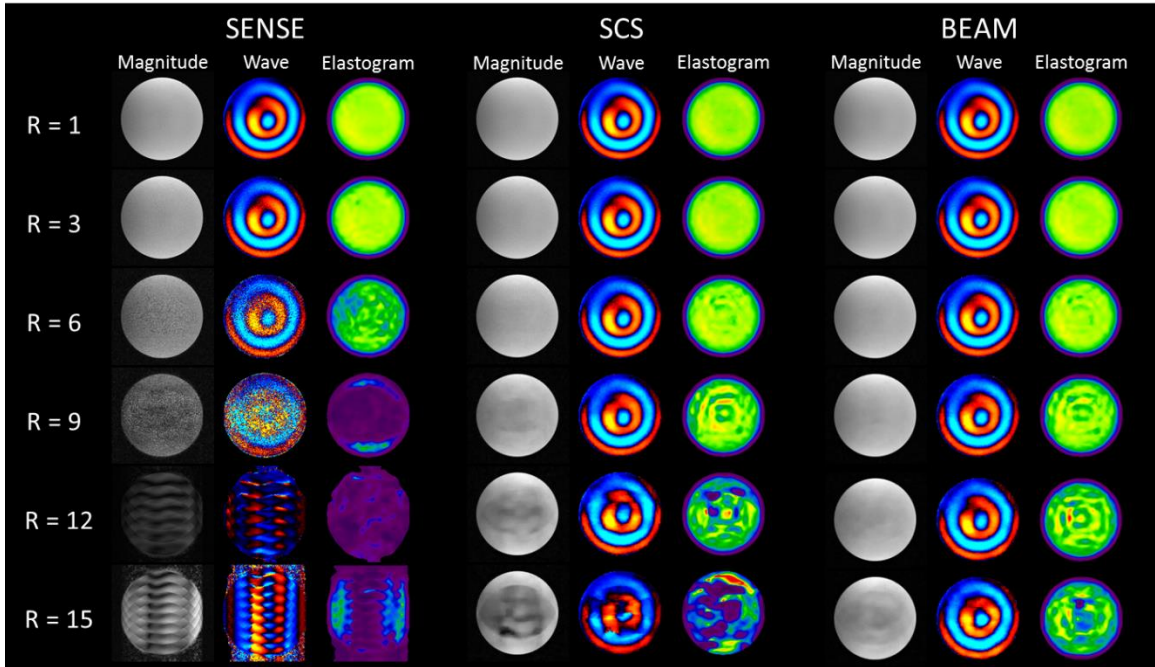


**Figure 8:** Comparison of SENSE, SCS, and BEAM phantom reconstructions at  $R = 1, 3, 6, 9, 12,$  and  $15$ . Magnitude images, wave images, and elastograms are shown for each reconstruction.

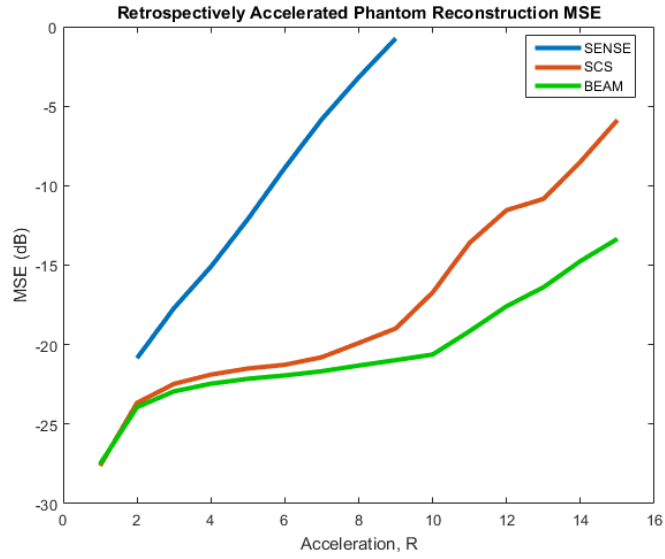


**Figure 9:** MSE of reconstructed phantom images for SENSE, SCS, and BEAM reconstructions. MSE provides a measure of the error between each complex reconstruction and the fully sampled SENSE reconstruction.

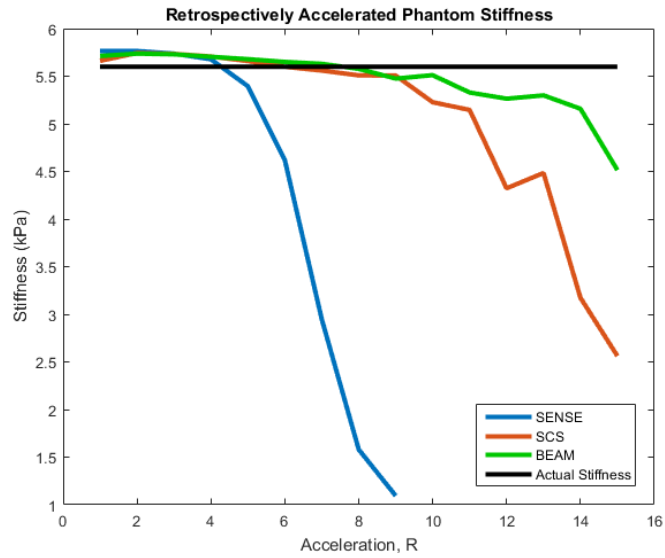


**Figure 10:** Mean phantom stiffness, as measured from the ROI.

## Prospectively Accelerated In Vivo Liver MRE Results

For prospectively accelerated data, **Figure 11** depicts GRAPPA and BEAM magnitude images, wave images, and elastograms for one of the volunteers. **Figure 12** shows Bland Altman analysis of stiffness estimates between GRAPPA and BEAM with different acceleration rates. Compared to the stiffness values derived from GRAPPA  $R = 1.4$ , the BEAM derived values at  $R = 1, 4, 6,$  and  $8$  yield biases of  $-0.06, -0.07, -0.04,$  and  $-0.06,$  respectively. The limits of agreement between GRAPPA and BEAM derived stiffness values are  $-0.35 — 0.23, -0.36 — 0.21, -0.36 — 0.28,$  and  $-0.46 — 0.33,$  respectively. Pearson correlation coefficients between BEAM and GRAPPA-derived stiffness values were  $0.831, 0.821, 0.800,$  and  $0.637$  for  $R=1, 4, 6,$  and  $8,$  respectively.

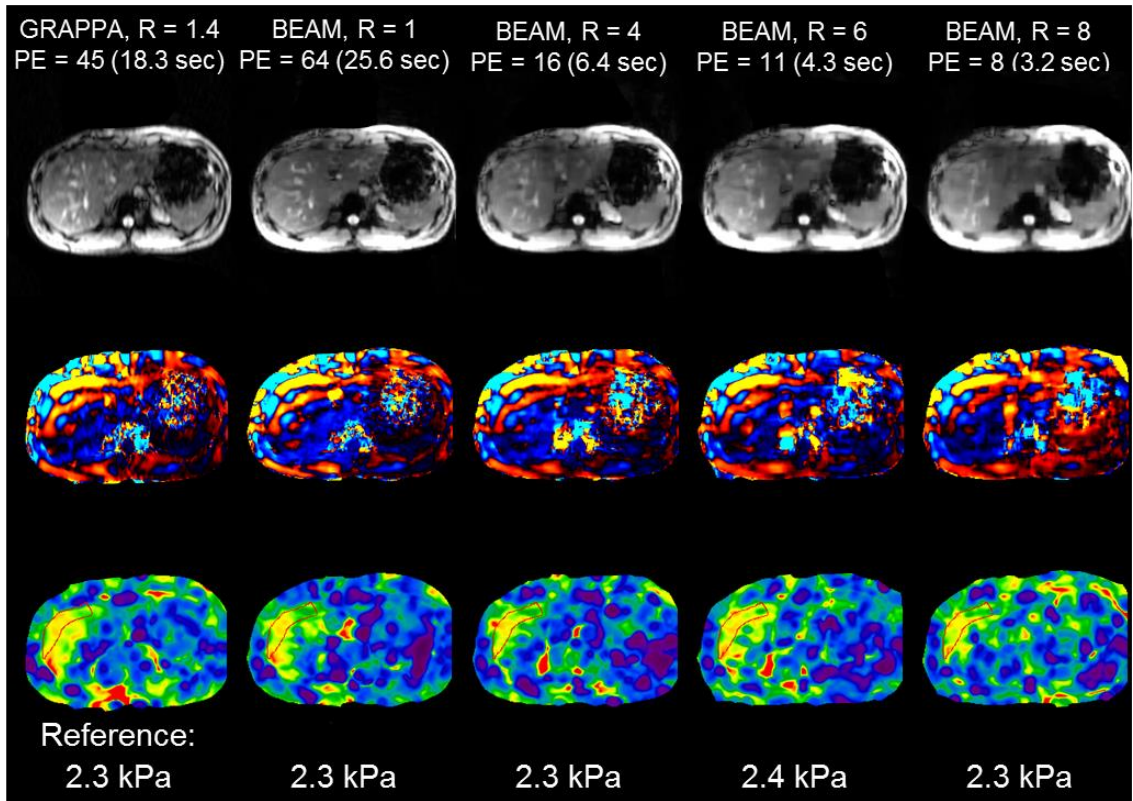


**Figure 11:** Comparison of GRAPPA at R = 1.4 and BEAM at R = 1, 4, 6, and 8 reconstructions of a representative prospectively accelerated in vivo dataset.

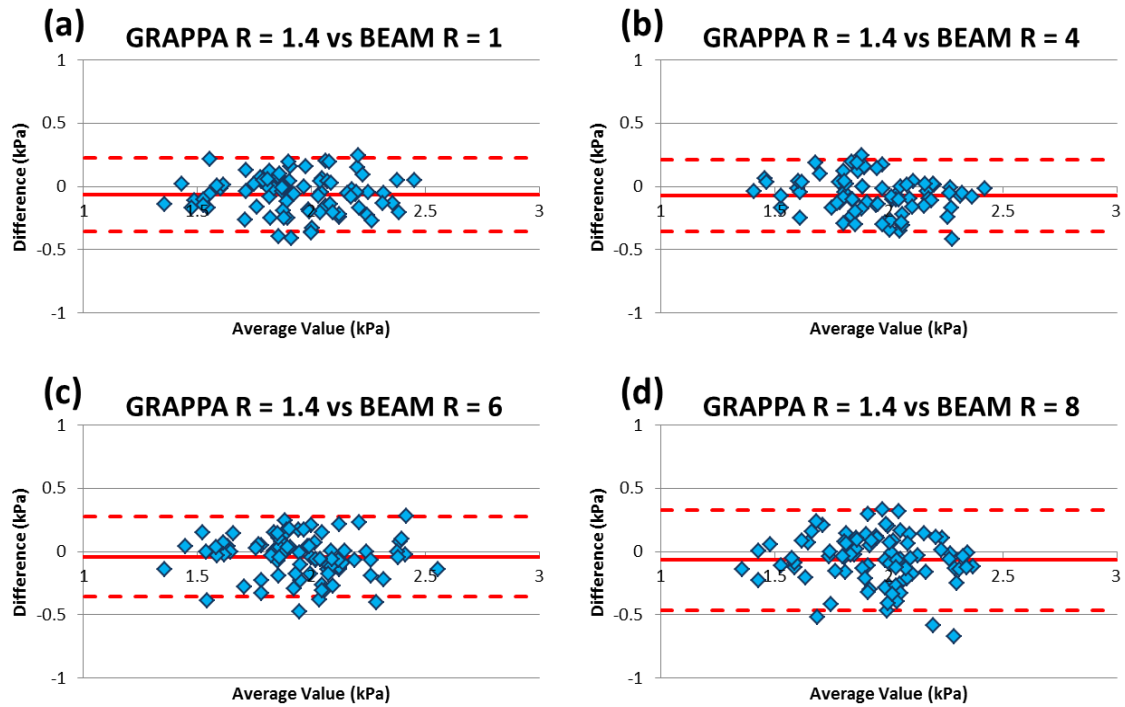


**Figure 12:** Bland Altman analysis of BEAM-derived stiffness measurements to GRAPPA-derived stiffness measurements. (a) Comparison of GRAPPA, R = 1.4, and BEAM, R = 1. (b) Comparison of GRAPPA, R = 1.4, and BEAM, R = 4. (c) Comparison of GRAPPA, R = 1.4, and BEAM, R = 6. (d) Comparison of GRAPPA, R = 1.4, and BEAM, R = 8.

Additionally, Bland Altman analysis (**Figure 13**) provided insight into the relationship between stiffness measurements derived from two subsequent GRAPPA acquisitions with identical parameters but collected under separate breath holds. The difference between the measurements demonstrated a bias of -0.04 and limits of agreement of -0.32 — 0.23. The correlation between the subsequent GRAPPA-derived stiffness measurements was 0.86.

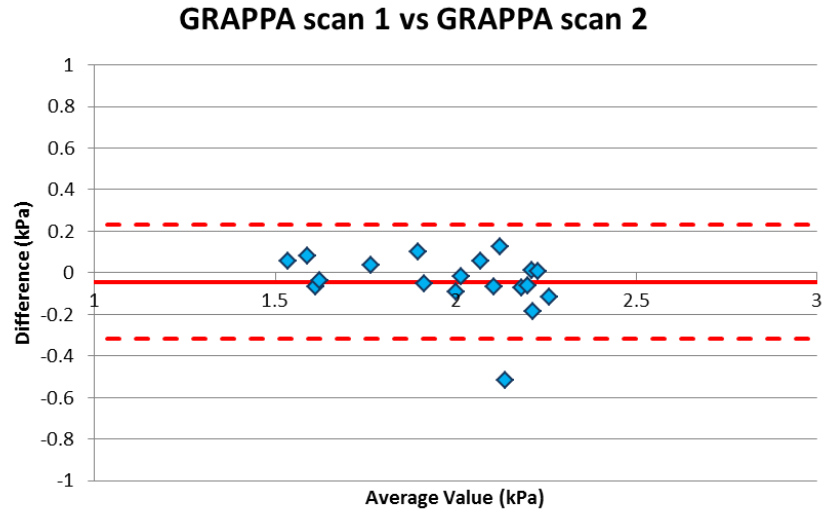


**Figure 13:** Bland Altman analysis of stiffness measurements derived from two separate GRAPPA scans. The two GRAPPA scans were collected from the same volunteer using identical parameters but under separate breath holds.

## Chapter 7: Discussion

The proposed acquisition and reconstruction strategy for MRE utilizes parallel MRI, spatial compressed sensing, and magnitude regularization across MRE phase offsets to enable image reconstruction at high acceleration rates without sacrificing image fidelity. In the phantom data, BEAM demonstrated significant improvement over SENSE reconstruction in MSE, and produced very high quality reconstructions for acceleration rates as high as  $R = 10$ . In the liver data, BEAM at  $R = 6$  exhibited high levels of agreement with GRAPPA at  $R = 1.4$ . Additionally, BEAM at  $R = 6$  demonstrated similar variation in performance compared to repeated GRAPPA scans.

BEAM exploits both spatial sparsity (in the wavelet domain) and magnitude consistency to enable image recovery from undersampled data. For magnitude consistency, BEAM utilizes a mixture density with hidden indicator variable to automatically adjust the extent of magnitude consistency on per-pixel basis. This probabilistic approach demonstrates significant improvement over application of a single magnitude constraint. In contrast, enforcing strict magnitude equality across all offsets led to significant image artifacts

(data not shown). Also, with a computationally efficient approximate message passing algorithm, BEAM enabled image recovery in less than 8 minutes using ordinary CPU-based computation. Further reduction in computation time is feasible by optimizing the code and by employing parallel computing.

In reconstruction of the retrospectively accelerated phantom, BEAM achieved the lowest MSE of all accelerated reconstructions considered, enabling acceleration rates as high as  $R = 10$  without substantially impacting results. At acceleration rates exceeding  $R = 4$ , BEAM provides an improvement over SCS of approximately 1 dB, which increases to more than 5 dB beyond  $R = 10$ . Both SCS and BEAM produce stiffness errors of less than 0.25 kPa (4%) for accelerations up to  $R = 9$ . At  $R = 10$  and beyond, BEAM demonstrated significant improvement over SCS in reconstruction stiffness measurements. Compared to MSE, mean stiffness is a more forgiving metric, which can explain the lack of performance loss for SCS until  $R=10$ . Compared to BEAM and SCS, SENSE reconstruction exhibits excessive noise amplification even at lower acceleration rates and degrades rapidly beyond  $R=4$ .

At low acceleration rates, BEAM effectively reduced the noise seen in smooth regions of the liver without sacrificing detail in vessels. These details are mostly preserved through  $R = 6$ , while images at  $R=8$  demonstrate visible reduction in fine detail. On average, across all in vivo datasets, the BEAM reconstruction at  $R = 6$  yielded a stiffness estimate which differs from the GRAPPA derived stiffness by 6.5%. From Bland Altman analysis,

stiffness measurements resulting from all four tested BEAM acceleration rates demonstrated no appreciable bias, as compared with GRAPPA at  $R = 1.4$ . A strong agreement ( $r \geq 0.8$ ) between BEAM ( $R \leq 6$ ) and GRAPPA at  $R = 1.4$  is observed. At  $R=8$ , however, the correlation degrades to  $r=0.68$ .

We conjecture that some of the variation between BEAM and GRAPPA at  $R = 1.4$  was due to small differences between the subsequent breath holds. Since each scan was performed under a separate breath hold, slight variation was introduced in the slice location of each scan, leading to small discrepancies in the resulting stiffness estimates. This conjecture is supported by the fact that Bland Altman for repeated GRAPPA measurements demonstrated very similar bias and limits of agreement as GRAPPA-BEAM analysis up to  $R = 6$ .

As implemented, BEAM reconstruction requires manual tuning of several parameters. Of principal importance are the Laplace shape parameter  $\lambda$ , controlling the tradeoff between data fidelity and wavelet compression, and the variance of the components of the mixture density  $\sigma_1^2$  and  $\sigma_2^2$ , controlling the strength of the two magnitude constraints across offsets. The values of these parameters were manually tuned using separate training datasets that were not included in the subsequent validation. For all phantom and in vivo datasets, we used  $\lambda = 20$  and observed that the recovery process was relatively robust to the choice of  $\lambda$ . For  $\sigma_1^2$  and  $\sigma_2^2$ , selecting small values generated lower MSE but provided inconsistent performance across different training datasets. To favor robustness over

optimality, we selected relatively large values  $\sigma_1^2$  and  $\sigma_2^2$ . Being a Bayesian approach, BEAM is amenable to auto-tuning using expectation maximization (64–66) or similar algorithms. Such extensions of BEAM are beyond the scope of current work and will be considered separately.

Several simplifications are made in the derivation of BEAM to ensure the algorithm is tractable and computationally efficient. To produce a tractable prior three independence assumptions are made. First, it is assumed that the location of magnitude discrepancies is independent of the complex-valued images. Second, the motion-encoded phase for each offset is independent of the magnitude and phase of each other offset, as well as the location of motion. Finally, it is assumed that each offset is independent of each other offset except the reference offset, eliminating loops in the factor graph between offsets while maintaining the structure used to enforce the magnitude regularization.

Additionally, two simplifications are made in the derivation of messages passed between offsets to enable processing of datasets consisting of numerous offsets. According to the sum-product algorithm (57), the message received by each offset consists of the product of the messages sent from each of the other offsets. These messages contain the mixture density, which is the sum of two circularly symmetric Rician terms. Thus, if  $J$  offsets are acquired (including all MEG offsets and polarities), the received message consists of a  $2^{J-1}$  term polynomial. To address this concern, cross terms involving multiplication between circularly symmetric Rician distributions with differing variances are disregarded, yielding messages consisting of the sum of two products of  $J - 1$

distributions. Additionally, the product of two Rician distributions is simplified as Rician, analogous to the product of two Gaussian distributions. This allows rapid, computationally efficient characterization of the messages through multiplications involving the mean and variance of each mixture density.

Numerous other potential applications of BEAM exist. Acceleration due to BEAM potentially permits acquisition of volumetric MRE within a single breath hold, which, in turn, enables further acceleration through compression in three spatial dimensions via a three dimensional wavelet transform. Alternatively, further compression could be achieved through leveraging the smooth structure of the liver with alternative sparsifying transforms such as curvelets or contourlets (67–70). BEAM is also amenable to multidimensional motion encoding, which provides a more complete depiction of the mechanical wave propagation through the region of interest by application of an MEG in three orthogonal spatial directions. Furthermore, exploration of alternative temporal encoding schemes, such as collection of seven MRE phase offsets, where only one offset includes negative motion encoding, could provide more accurate motion encoding.

All participants in this study were healthy volunteers with no history of liver disease. Future testing of BEAM in clinical patients could investigate the possibility of proportional bias at higher liver stiffness and validate the method against biopsy. After demonstrating success in staging liver fibrosis, BEAM could be assessed for detection

and staging of a variety of other diseases. The preliminary data strongly suggests that BEAM is a viable option to accelerate clinical application of liver MRE.

## Chapter 8: Conclusion

An acquisition and reconstruction strategy was presented for magnetic resonance elastography which enabled high rates of acceleration by utilizing spatially varying magnitude regularization across offsets, spatial sparsity, and accelerated computation via generalized approximate message passing. The algorithm, BEAM, was validated through reconstruction of retrospectively accelerated phantom as well as prospectively accelerated in vivo stiffness measurements in the liver. Stiffness measurements derived from prospectively accelerated BEAM reconstructions (at  $R = 6$ ) demonstrated strong consistency with stiffness measurements derived from GRAPPA  $R = 1.4$  reconstructions, with correlation coefficient  $r = 0.8$ . Thus, BEAM demonstrates potential for clinical elastography applications.

## References

1. Muthupillai R, Lomas D, Rossman P, Greenleaf J, Manduca A, Ehman R. Magnetic resonance elastography by direct visualization of propagating acoustic strain waves. *Science* (80-. ). 1995;269:1854–1857. doi: 10.1126/science.7569924.
2. Dulai PS, Sirlin CB, Loomba R. MRI and MRE for non-invasive quantitative assessment of hepatic steatosis and fibrosis in NAFLD and NASH: Clinical trials to clinical practice. *J. Hepatol.* 2016;65:1006–1016. doi: 10.1016/j.jhep.2016.06.005.
3. Yasar TK, Wagner M, Bane O, Besa C, Babb JS, Kannengiesser S, Fung M, Ehman RL, Taouli B. Interplatform reproducibility of liver and spleen stiffness measured with MR elastography. *J. Magn. Reson. Imaging* 2016;43:1064–1072. doi: 10.1002/jmri.25077.
4. Petittlerc L, Sebastiani G, Gilbert G, Cloutier G, Tang A. Liver fibrosis: Review of current imaging and MRI quantification techniques. *J. Magn. Reson. Imaging* 2016. doi: 10.1002/jmri.25550.

5. Glaser KJ, Manduca A, Ehman R. Review of MR elastography applications and recent developments. *J. Magn. Reson. Imaging* 2012;36:757–774. doi: 10.1002/jmri.23597.
6. Wassenaar PA, Eleswarpu CN, Schroeder SA, Mo X, Raterman BD, White RD, Kolipaka A. Measuring age-dependent myocardial stiffness across the cardiac cycle using MR elastography: A reproducibility study. *Magn. Reson. Med.* 2016;75:1586–1593. doi: 10.1002/mrm.25760.
7. Mazumder R, Schroeder S, Mo X, Clymer BD, White RD, Kolipaka A. In vivo quantification of myocardial stiffness in hypertensive porcine hearts using MR elastography. *J. Magn. Reson. Imaging* 2016. doi: 10.1002/jmri.25423.
8. Hawley JR, Kalra P, Mo X, Raterman B, Yee LD, Kolipaka A. Quantification of breast stiffness using MR elastography at 3 Tesla with a soft sternal driver: A reproducibility study. *J. Magn. Reson. Imaging* 2016:1379–1384. doi: 10.1002/jmri.25511.
9. Damughatla AR, Raterman B, Sharkey-Toppen T, Jin N, Simonetti OP, White RD, Kolipaka A. Quantification of aortic stiffness using MR elastography and its comparison to MRI-based pulse wave velocity. *J. Magn. Reson. Imaging* 2015;41:44–51. doi: 10.1002/jmri.24506.
10. Kolipaka A, Illapani VSP, Kenyhercz W, Dowell JD, Go MR, Starr JE, Vaccaro PS, White RD. Quantification of abdominal aortic aneurysm stiffness using magnetic

resonance elastography and its comparison to aneurysm diameter. *J. Vasc. Surg.* [Internet] 2016;64:966–974. doi: 10.1016/j.jvs.2016.03.426.

11. Wang J, Malik N, Yin M, Smyrk TC, Czaja AJ, Ehman RL, Venkatesh SK. Magnetic resonance elastography is accurate in detecting advanced fibrosis in autoimmune hepatitis. *World J. Gastroenterol.* 2017;23:859–868. doi: 10.3748/wjg.v23.i5.859.

12. Yin M, Talwalkar JA, Glaser KJ, Manduca A, Grimm RC, Rossman PJ, Fidler JL, Ehman RL. Assessment of Hepatic Fibrosis With Magnetic Resonance Elastography. *Clin. Gastroenterol. Hepatol.* 2007;5:1207–1213. doi: 10.1016/j.cgh.2007.06.012.

13. Sanyal AJ. AGA technical review on nonalcoholic fatty liver disease. *Gastroenterology* 2002;123:1705–1725. doi: 10.1053/gast.2002.36572.

14. Kleiner DE, Brunt EM, Van Natta M, et al. Design and validation of a histological scoring system for nonalcoholic fatty liver disease. *Hepatology* 2005;41:1313–1321. doi: 10.1002/hep.20701.

15. Mulhall BP, Ong JP, Younossi ZM. Non-alcoholic fatty liver disease: an overview. *J. Gastroenterol. Hepatol.* 2002;17:1136–43. doi: 10.1046/j.1440-1746.2002.02881.x.

16. Schuppan D, Afdhal NH. Liver cirrhosis. *Lancet* 2008;371:838–851. doi: 10.1016/S0140-6736(08)60383-9.

17. Kochanek KD, Murphy SL, Xu J, Tejada-Vera B. Deaths : Final Data for 2010. *Natl. Vital Stat. Reports* 2016;65.
18. Afdhal NH, Nunes D. Evaluation of liver fibrosis: A concise review. *Am. J. Gastroenterol.* 2004;99:1160–1174. doi: 10.1111/j.1572-0241.2004.30110.x.
19. Standish RA. An appraisal of the histopathological assessment of liver fibrosis. *Gut* 2006;55:569–578. doi: 10.1136/gut.2005.084475.
20. Bravo AA, Sheth SG, Chopra S. Liver Biopsy. *N. Engl. J. Med.* 2001;344:495–500.
21. Cholongitas E, Senzolo M, Standish R, Marelli L, Quaglia A, Patch D, Dhillon AP, Burroughs AK. A systematic review of the quality of liver biopsy specimens. *Am J Clin Pathol* 2006;125:710–721. doi: 10.1309/W3XC-NT4H-KFBN-2G0B.
22. Dienstag JL. The role of liver biopsy in chronic hepatitis C. *Hepatology* 2002;36:S152-60. doi: 10.1053/jhep.2002.36381.
23. Gerstenmaier JF, Gibson RN. Ultrasound in chronic liver disease. *Insights Imaging* 2014;5:441–455. doi: 10.1007/s13244-014-0336-2.
24. Vessal S, Naidoo S, Hodson J, Stella D, Gibson R. Hepatic Vein Morphology. 2009:1219–1227.
25. Castera L, Forns X, Alberti A. Non-invasive evaluation of liver fibrosis using

transient elastography. *J. Hepatol.* 2008;48:835–847. doi: 10.1016/j.jhep.2008.02.008.

26. Friedrich-Rust M, Ong MF, Martens S, Sarrazin C, Bojunga J, Zeuzem S, Herrmann E. Performance of Transient Elastography for the Staging of Liver Fibrosis: A Meta-Analysis. *Gastroenterology* 2008;134:960–974. doi: 10.1053/j.gastro.2008.01.034.

27. Friedrich-Rust M, Nierhoff J, Lupsor M, et al. Performance of Acoustic Radiation Force Impulse imaging for the staging of liver fibrosis: A pooled meta-analysis. *J. Viral Hepat.* 2012;19:212–219. doi: 10.1111/j.1365-2893.2011.01537.x.

28. Franchi-Abella S, Elie C, Correas JM. Ultrasound elastography: Advantages, limitations and artefacts of the different techniques from a study on a phantom. *Diagn. Interv. Imaging* 2013;94:497–501. doi: 10.1016/j.diii.2013.01.024.

29. Koinuma M, Ohashi I, Hanafusa K, Shibuya H. Apparent diffusion coefficient measurements with diffusion-weighted magnetic resonance imaging for evaluation of hepatic fibrosis. *J. Magn. Reson. Imaging* 2005;22:80–85. doi: 10.1002/jmri.20344.

30. Wang QB, Zhu H, Liu HL, Zhang B. Performance of magnetic resonance elastography and diffusion-weighted imaging for the staging of hepatic fibrosis: A meta-analysis. *Hepatology* 2012;56:239–247. doi: 10.1002/hep.25610.

31. Mariappan YK, Glaser KJ, Ehman RL. Magnetic resonance elastography: A review. *Clin. Anat.* 2010;23:497–511. doi: 10.1002/ca.21006.

32. Abe H, Midorikawa Y, Mitsuka Y, et al. Predicting postoperative outcomes of liver resection by magnetic resonance elastography. *Surgery* 2017;1–8. doi: 10.1016/j.surg.2017.02.014.
33. Gharib AM, Ai M, Han T, et al. Magnetic Resonance Elastography Shear Wave Velocity Correlates with Liver Fibrosis and Hepatic Venous Pressure Gradient in Adults with Advanced Liver Disease. 2017;2017.
34. Hiscox L V, Johnson CL, Barnhill E, McGarry MDJ, Huston J, van Beek EJR, Starr JM, Roberts N. Magnetic resonance elastography (MRE) of the human brain: technique, findings and clinical applications. *Phys. Med. Biol.* [Internet] 2016;61:R401–R437. doi: 10.1088/0031-9155/61/24/R401.
35. Plewes DB, Bishop J, Samani A, Sciarretta J. Visualization and quantification of breast cancer biomechanical properties with magnetic resonance elastography  
Visualization and quantification of breast cancer biomechanical properties with magnetic resonance elastography. *Phys. Med. Biol.* 2000;1591.
36. Low G, Kruse SA, Lomas DJ. General review of magnetic resonance elastography. *World J. Radiol.* 2016;8:59–72. doi: 10.4329/wjr.v8.i1.59.
37. Feng Y, Clayton EH, Okamoto RJ, Engelbach J, Bayly P V, Garbow JR. A longitudinal magnetic resonance elastography study of murine brain tumors following

radiation therapy. *Phys. Med. Biol.* [Internet] 2016;61:6121. doi: 10.1088/0031-9155/61/16/6121.

38. Arunachalam SP, Arani A, Baffour F, et al. Regional assessment of in vivo myocardial stiffness using 3D magnetic resonance elastography in a porcine model of myocardial infarction. *Magn. Reson. Med.* 2017;0. doi: 10.1002/mrm.26695.

39. Skerl K, Vinnicombe S, Thomson K, McLean D, Giannotti E, Evans A. Anisotropy of Solid Breast Lesions in 2D Shear Wave Elastography is an Indicator of Malignancy. *Acad. Radiol.* 2016;23:53–61. doi: 10.1016/j.acra.2015.09.016.

40. Zhang N, Chen J, Yin M, Glaser KJ, Xu L, Ehman RL. Quantification of regional aortic stiffness using MR elastography: A phantom and ex-vivo porcine aorta study. *Magn. Reson. Imaging* 2016;34:91–96. doi: 10.1016/j.mri.2015.10.011.

41. Nelissen JL, Elastography MR, Nelissen JL. A MRI-Compatible Combined Mechanical Loading and MR Elastography Setup to Study Deformation-Induced Skeletal Muscle Damage in Rats. *PLoS One* 2017;12. doi: 10.1371/journal.pone.0169864.

42. Huwart L, Sempoux C, Vicaud E, et al. Magnetic Resonance Elastography for the Noninvasive Staging of Liver Fibrosis. *Gastroenterology* 2008;135:32–40. doi: 10.1053/j.gastro.2008.03.076.

43. Venkatesh SK, Yin M, Ehman RL. Magnetic resonance elastography of liver:

technique, analysis, and clinical applications. *J. Magn. Reson. Imaging* 2013;37:544–55. doi: 10.1002/jmri.23731.

44. Chamarthi SK, Raterman B, Mazumder R, Michaels A, Oza VM, Hanje J, Bolster B, Jin N, White RD, Kolipaka A. Rapid acquisition technique for MR elastography of the liver. *Magn. Reson. Imaging* 2014;32:679–683. doi: 10.1016/j.mri.2014.02.013.

45. Manduca A, Lake DS, Kruse SA, Ehman RL. Spatio-temporal directional filtering for improved inversion of MR elastography images. *Med. Image Anal.* 2003;7:465–473. doi: 10.1016/S1361-8415(03)00038-0.

46. Knutsson H, Westin CF, Granlund G. Local multiscale frequency and bandwidth estimation. *Proc. - Int. Conf. Image Process. ICIP* 1994;1:36–40. doi: 10.1109/ICIP.1994.413270.

47. Dzyubak B, Venkatesh SK, Manduca A, Glaser KJ, Ehman RL. Automated liver elasticity calculation for MR elastography. *J. Magn. Reson. Imaging* 2016;43:1055–1063. doi: 10.1002/jmri.25072.

48. Silva AM, Grimm RC, Glaser KJ, Fu Y, Wu T, Ehman RL, Silva AC. Magnetic resonance elastography: evaluation of new inversion algorithm and quantitative analysis method. *Abdom. Imaging* 2015;40:810–817. doi: 10.1007/s00261-015-0372-5.

49. Ting ST, Ahmad R, Jin N, Craft J, Serafim da Silveira J, Xue H, Simonetti OP. Fast

implementation for compressive recovery of highly accelerated cardiac cine MRI using the balanced sparse model. *Magn. Reson. Med.* 2016;1515:1505–1515. doi:

10.1002/mrm.26224.

50. Feng L, Benkert T, Block KT, Sodickson DK, Otazo R, Chandarana H. Compressed sensing for body MRI. *J. Magn. Reson. Imaging* 2016. doi: 10.1002/jmri.25547.

51. Ge W, Bresler Y, Ntziachristos V. Guest Editorial Compressive Sensing for Biomedical Imaging. *Med. Imaging, IEEE Trans.* 2011;30:1013–1016. doi:

10.1109/tmi.2011.2145070.

52. Otazo R, Kim D, Axel L, Sodickson DK. Combination of compressed sensing and parallel imaging for highly accelerated first-pass cardiac perfusion MRI. *Magn. Reson. Med.* 2010;64:767–776. doi: 10.1002/mrm.22463.

53. Murphy M, Alley M, Demmel J, Keutzer K, Vasanawala S, Lustig M. Fast  $l_1$  - SPIRiT compressed sensing parallel imaging MRI: scalable parallel implementation and clinically feasible runtime. *IEEE Trans. Med. Imaging* 2012;31:1250–62. doi:

10.1109/TMI.2012.2188039.

54. Rich A, Potter LC, Jin N, Ash J, Simonetti OP, Ahmad R. A Bayesian model for highly accelerated phase-contrast MRI. *Magn. Reson. Med.* 2016;76:689–701. doi:

10.1002/mrm.25904.

55. Ahmad R, Xue H, Giri S, Ding Y, Craft J, Simonetti OP. Variable density incoherent spatiotemporal acquisition (VISTA) for highly accelerated cardiac MRI. *Magn. Reson. Med.* 2015;74:1266–78. doi: 10.1002/mrm.25507.
56. Borgerding M, Schniter P, Vila J, Rangan S. Generalized approximate message passing for cospase analysis compressive sensing. *Acoust. Speech Signal Process. (ICASSP), 2015 IEEE Int. Conf.* 2015;43210:3756–3760. doi: 10.1109/ICASSP.2015.7178673.
57. Kschischang FR, Frey BJ, Loeliger HA. Factor graphs and the sum-product algorithm. *IEEE Trans. Inf. Theory* 2001;47:498–519. doi: 10.1109/18.910572.
58. Loeliger HA, Dauwels J, Hu J, Korl S, Ping L, Kschischang FR. The factor graph approach to model-based signal processing. *Proc. IEEE* 2007;95:1295–1322. doi: 10.1109/JPROC.2007.896497.
59. Rangan S. Generalized approximate message passing for estimation with random linear mixing. *Inf. Theory Proc. (ISIT), 2011 IEEE Int. Symp.* 2010:2168–2172. doi: 10.1109/ISIT.2011.6033942.
60. Pruessmann KP, Weiger M, Scheidegger MB, Boesiger P. SENSE: Sensitivity encoding for fast MRI. *Magn. Reson. Med.* 1999;42:952–962. doi: 10.1002/(SICI)1522-2594(199911)42:5<952::AID-MRM16>3.0.CO;2-S.

61. Griswold MA, Jakob PM, Heidemann RM, Nittka M, Jellus V, Wang J, Kiefer B, Haase A. Generalized Autocalibrating Partially Parallel Acquisitions (GRAPPA). *Magn. Reson. Med.* 2002;47:1202–1210. doi: 10.1002/mrm.10171.
62. Walsh DO, Gmitro AF, Marcellin MW. Adaptive reconstruction of phased array MR imagery. *Magn. Reson. Med.* 2000;43:682–690. doi: 10.1002/(SICI)1522-2594(200005)43:5<682::AID-MRM10>3.0.CO;2-G.
63. Altman DG, Bland JM. Measurement in Medicine : the Analysis of Method Comparison Studies. *Statistician* 1983;32:307–317. doi: 10.2307/2987937.
64. Dempster AP, Laird NM, Rubin DB. Maximum likelihood from incomplete data via the EM algorithm. *J. R. Stat. Soc. Ser. B Methodol.* 1977;39:1–38. doi: <http://dx.doi.org/10.2307/2984875>.
65. Mahjoub MA, Bouzaiene A, Ghanmy N. Tutorial and selected approaches on parameter learning in bayesian network with incomplete data. *Adv. Neural Networks* 2012;7367 LNCS:478–488. doi: 10.1007/978-3-642-31346-2\_54.
66. Vila JP, Schniter P. Expectation-Maximization Gaussian-Mixture Approximate Message Passing. *IEEE Trans. Signal Process.* 2013;61:1–15.
67. Qu X, Guo D, Chen Z, Cai C. Compressed sensing MRI based on nonsubsampling contourlet transform. *Proc. 2008 IEEE Int. Symp. IT Med. Educ. ITME 2008* 2008:693–

696. doi: 10.1109/ITME.2008.4743955.

68. Wangli H, Jianwu L, Xiaobo Q, Zhengchao D. Fast iterative contourlet thresholding for compressed sensing MRI. *Electron. Lett.* 2013;49:1206–1208. doi: 10.1049/el.2013.1483.

69. Qu X, Cao X, Guo D, Hu C, Chen Z. Combined sparsifying transforms for compressed sensing MRI. *Electron. Lett.* 2010;46:121. doi: 10.1049/el.2010.1845.

70. Donoho DL, Duncan MR. Digital curvelet transform: strategy, implementation, and experiments. *Proc. SPIE* 1999;4056:12–30. doi: 10.1117/12.381679.